RESEARCH PAPER

Microstructure evaluation of dissimilar AA2024 and AA7050 aluminum joints made by corner stationary-shoulder friction stir welding

V. Mertinger[1] · B. Varbai[2] · Y. Adonyi[3] · J. DeBacker[4] · E. Nagy[1] · M. Leskó[1] · V. Kárpáti[1]

Abstract

Fillet welds made by the corner stationary-shoulder friction stir welding process between AA7050-T7451 and AA2024-T4 sheets were characterized using different metallographic techniques and mechanical testing. Robotic welds of an aircraft's skin-to-internal stiffeners were examined using Barker's electrolytic and Keller's etching techniques and correlated with electron backscattered diffraction results and energy-dispersive microprobe analysis. The composition and grain orientation maps and material flow lines demonstrated excellent weld quality in spite of the apparent inhomogeneities in the stir zone where mechanical mixing was complete. Welded joint efficiencies were in the 85–92% of the base metals and were acceptable in terms of resistance to crack initiation and propagation and corrosion resistance, even with softening of the heat-affected zones. It was concluded that several optical and electron microscopy techniques are needed to characterize these dissimilar aluminum welds fully and that post-weld mechanical and thermal treatments could even further improve their quality.

Keywords Friction stir welding (FSW) · Dissimilar aluminum joints · Stationary shoulder friction stir welding (SS-FSW) · Corner stationary shoulder friction stir welding (CSS-FSW)

1 Introduction

Joining internal reinforcements (stiffeners) to the aircraft skin for cargo doors is still performed by riveting in most commercial aircraft. However, fatigue and corrosion failures initiated at the holes produced in the process have prompted researchers to find welding alternatives to riveting, achieving cost reduction, and improved productivity [1]. Fusion welding alternatives to riveting had been abandoned many years ago due to heat-affected zone (HAZ) softening of the aluminum alloys involved [2, 3]. The effect of precipitate dissolution and grain growth could be improved by post-weld heat treatment (PWHT) [4–6], but practical limits to

✉ B. Varbai
varbai.balazs@gpk.bme.hu

[1] University of Miskolc, Miskolc, Hungary

[2] Budapest University of Technology and Economics, Budapest, Hungary

[3] University West, Trollhättan, Sweden

[4] TWI Ltd., Cambridge, UK

heat treating large subassemblies to the entire aircraft kept this solution from implementation. Therefore, fusion welding solutions were no longer considered, and new, solid-state welding solutions were investigated [7–9].

Friction stir welding (FSW) typically produces lower peak HAZ temperatures and results in less HAZ softening than fusion welds, showing great promise in replacing riveting [10]. After successful static and dynamic testing, Friction stir welds proved equal and sometimes superior to riveted joints [10–12]. For the Eclipse aircraft, a total weld length of 136 m consisting of 263 separate FSW welds replaced 7378 conventional rivets. Although no exact numbers were given, the authors claimed that welding was performed in "a fraction of the time" compared with mechanical fastening [13]. The need for new equipment and robotic welding fixtures and setups kept larger aircraft producers from moving toward FSW. In particular, good corrosion properties between dissimilar aluminum alloys could not be accomplished by the conventional low travel speed FSW process [14]. The corrosion resistance of the dissimilar welds between the 6xxx and 7xxx series aluminum alloys was further affected by the difference in precipitation behavior of Al-Zn precipitates [15–17].

Furthermore, the temperature induced by welding on the outer skin to be kept below 120 °C affected the paint and surface treatment. Finally, conventional FSW was only possible inside the structure, as the rough surface brought about aerodynamic resistance (turbulences) around the weld seams, requiring surface grinding after welding.

To further reduce the heat input for alloys with poor thermal conductivity, i.e., titanium alloys, a low-heat input variant of the FSW process was developed, consisting of a rotating probe and a non-rotating "stationary" shoulder (SS-FSW) [18]. This technique was later successfully applied to aluminum and light metal alloys [19–22]. The method not only offers significantly lower heat input and higher welding speeds but can also improve the weld top surface finish quality. SS-FSW also enables the welding of corner and fillet joints, which was impossible with conventional FSW. A schematic of corner stationary-shoulder FSW (CSS-FSW) and a typical cross-section of a CSS-FSW weld are shown in Fig. 1 [23], under the CornerStir™ patented process name by TWI Ltd.

With this modified FSW technique, all frictional heat is generated by the rotation of the probe at much higher rotational speeds than traditional FSW. While the conventional FSW tool typically rotates at 1000–2000 RPM for welding aluminum (where both the shoulder and the pin rotate at the same speed) [24–27], the SS-FSW probe rotates at 3000–5000 RPM while the shoulder is stationary. Accordingly, welding can progress faster and at lower heat inputs.

The CornerStir™ welding technique was applied to dissimilar welding of AA2024 and AA7050 aluminum alloys, a typical application in the aerospace industry. The AA2024 alloy acts as an anode, and the AA7050 alloy serves as a cathode in the electro galvanic cell, which describes the related corrosion mechanism [28]. Researchers showed that the friction stir–welded stir zone of these dissimilar joints could have the same corrosion resistance as the base material [29].

In the present application, these internally performed CSS-FSW fillet welds between the same two aluminum alloys were intended to replace approximately 500,000 rivets on an Airbus A350 plane, which at 4 g/rivet could save 2.0 metric tons in rivet weight alone. Combined with the weight savings of washers and sealants, the total weight savings per 135-ton aircraft could be 5–10% [30].

The present paper was intended to look more closely at these dissimilar aluminum CSS-FSW welds and provide more understanding of the microstructure-property relationships using a combination of analytical techniques and characterize the friction stir zone and heat affected zone microstructures.

2 Experimental processes and methodology

2.1 Materials, experimental design, and procedures

The CSS-FSW process was applied to produce an aircraft cargo door demonstrator for an Airbus 320-series, currently manufactured by SAAB Technologies in Sweden. A 2.8-mm-thick AA2024-T4 was used for the door skin, which was reinforced with 2.0-mm-thick AA7050-T7451 stiffeners. The alloys' nominal chemical compositions and mechanical properties are listed in Table 1.

Figure 2 shows the T-shaped stiffeners (purple) welded to the outer skin using robotic CSS-FSW welding at TWI Ltd. [30]. It is important to note that the T-frame was thickened in the joint area to provide the fillet throat material and compensate for variations in fit-up and gaps (Fig. 3).
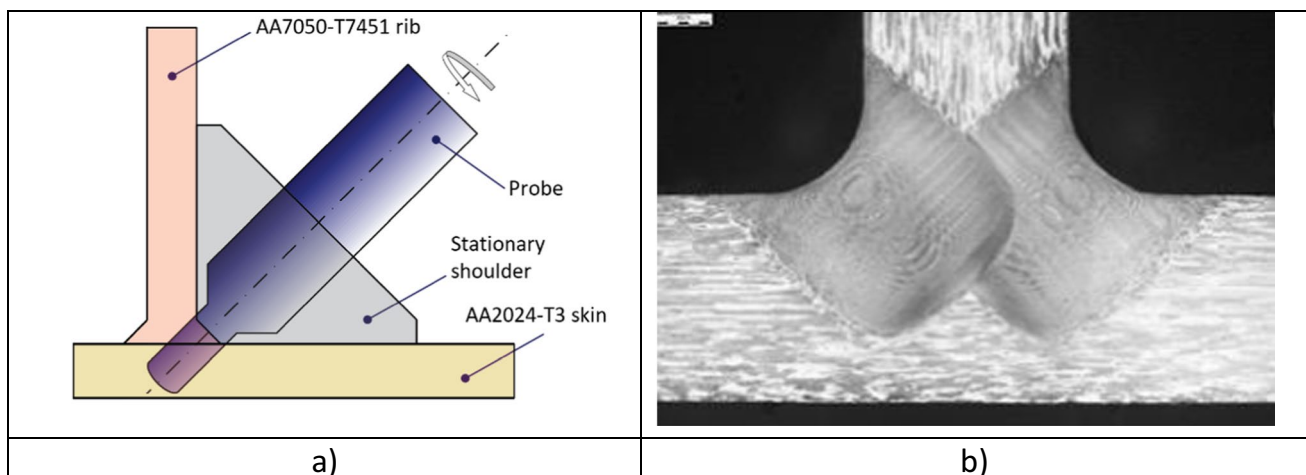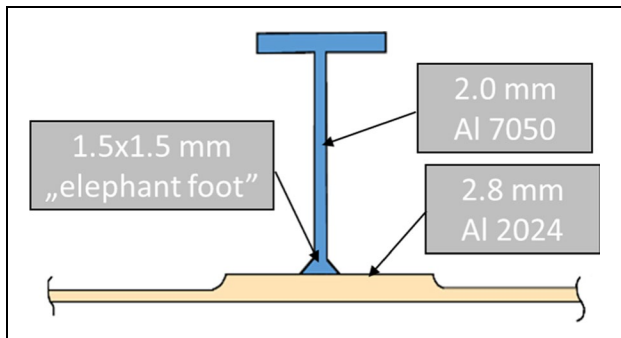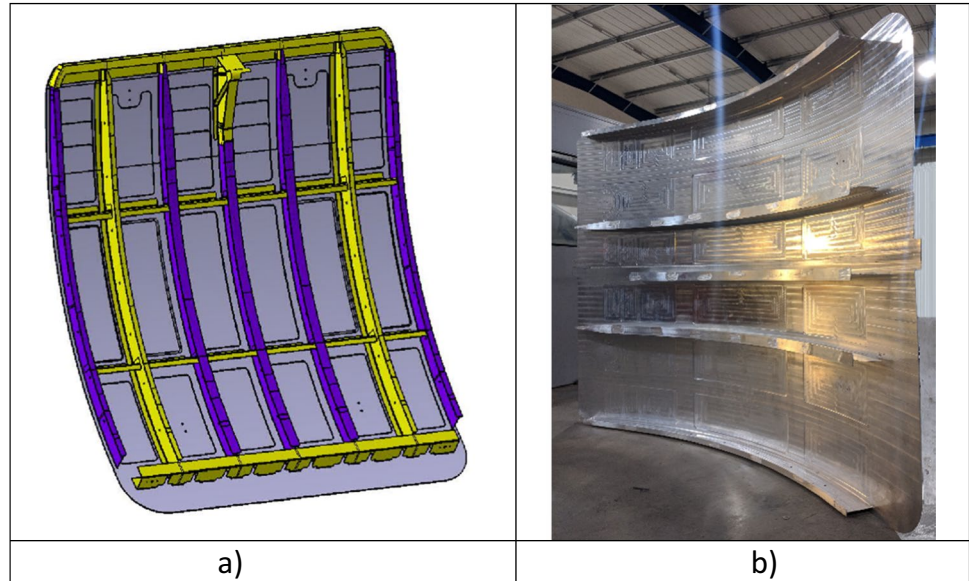

Fig. 1 **a** Schematic of the corner FSW process named "CornerStir™" (CSS-FSW), developed by TWI Ltd., **b** a typical cross-section through a CSS-FSW fillet weld [23]

Table 1 Nominal properties of the base metals

Alloy	Composition, wt%						Mechanical properties		
	Cu	Mg	Zn	Zr	Fe	Si	YS, MPa	UTS, MPa	Elongation, %
AA7050-T7451	2.23	2.25	6.2	0.12	<0.12	<0.15	490	550	17
AA2024-T4	4.29	1.37	0.16	0.08	<0.20	<0.20	345	480	14

Fig. 2 **a** Schematic of the aircraft door AA2024-T4 skin with AA7050-7451 stiffeners and **b** completely welded demonstrator piece, approximately 2×3 m in size

Fig. 3 Schematic of the special T-joint preparation prior to CSS FSW welding of the AA2024-T4 skin (lower member) and AA7050-T7451 internal reinforcement (vertical member)

The CornerStir™ CSS-FSW process was performed using the following typical parameters: rotational probe speed 3000 RPM and downforce 6000 N. The rotating inner probe material was a cobalt-based superalloy type M 159, while the shoulder was made of H-13 hardened tool steel.

Specific CornerStir™ tool design and dimensions used are proprietary to TWI Ltd., yet it is essential to note that the tool cost less than 100 Euros, and over 500 m of weld were made with one single tool. For these demos, a relatively low travel speed of 180 mm/min was used, even though the SS-FSW process, in general, is capable of rates one order of magnitude higher in lap configurations and where the tool downforce can be increased to 10 000 N. For the robotic setup, these optimum settings were not possible due to system limitations, hence the relatively low travel speeds used for the experiments.

It is believed that after the prototype door passes full-scale testing, the industrial gantry setup will be capable of CSS FSW welding at higher speeds. The angle between the CSS-FSW welding head and the normal to the welding direction was varied between 0.5, 1, and 1.5° from the vertical. The robotic welding system used is shown in Fig. 4.

2.2 Characterization

A static T-pull test was performed on welded and heat-treated specimens to qualify the mechanical bonding of the weld at VZLU, Prague, Czech Republic. During the T-pull test, the AA2024 plate was fixed, and the AA7050 plate was subjected to tensile load. For each condition, 4–4 parallel tests were performed. A photo of the test is shown in Fig. 5.

Because initial etching revealed potential failure sites near the heat-affected zone and at an apparent oxide inclusion in the stir zone, two additional types (A and B) of unconventional bending tests were also performed on select welded specimens. The schematic image of the bending test
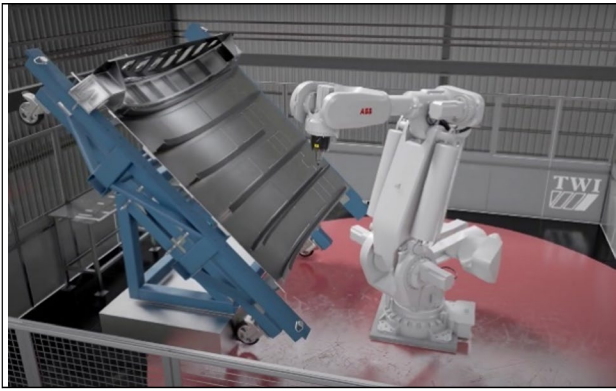
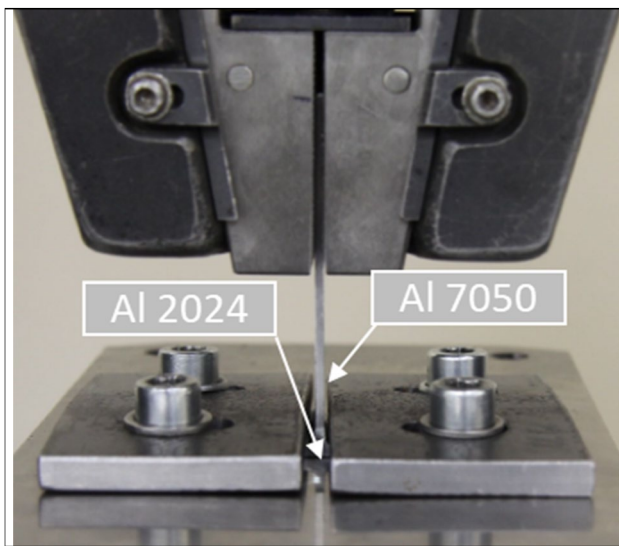Fig. 4 Robotic setup and particular fixture used for CSS FSW welding of the stiffeners to the outer skin

Fig. 5 Typical setup of the T-pull-test performed on the welded and heat-treated specimens

setups can be seen in Fig. 6. For the A-type bending test, one side of the AA7050-T7451 plate was machined off by grinding, so the corner weld could be opened and subjected to a compressive load (Fig. 7). For the B-type bending test, the AA7050-T7451 vertical member of the T-joint was
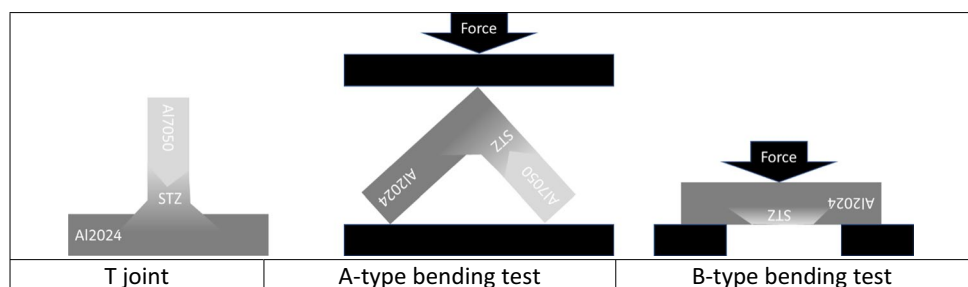
removed by grinding, so a three-point bending test could have been performed (L-shape sample). During the B-type bending test, the tensile load was applied to the surface, where the AA7050 member was removed from (bottom side in Fig. 8), so the interface between the two welding passes (e.g., Fig. 11) could have been opened to reveal internal defects such as oxide inclusions (flat plate sample). The distance between the supports was 25 mm, and the bending device was a V-block with a 10-mm radius.

Metallography was performed on transverse cross-sections using light optical microscopy (LOM) and scanning electron microscopy (SEM). Different etching agents were also used to reveal complex microstructural features as much detail as possible. Secondary electrons (SE) and backscattered electron (BSE) signals were used for imaging in the SEM system. Select welded samples were examined by using standard Keller's etching (mixing 2 ml hydrofluoric acid, 3 ml hydrochloric acid, 5 ml nitric acid, and 190 ml of distilled water) and Barker's electrolytic etching, performed using a mixture of 5 g of tetra-fluoboric acid dissolved in 200 ml of water, at 25 V electrical potential DC for 90 s. Polarized light microscopy (P-LOM) was used to document the grains' qualitative orientation and visualize the structural flow lines.

Mosaic images were used for both light and electron microscopy. A mosaic image is created by combining many high-resolution image sequences, thus achieving a panoramic view so that the image becomes rich in detail instead of a low-magnification image.

A Thermo Scientific Helios G4 plasma focused ion beam scanning electron microscopy (PFIB SEM) system was used for selective area electron backscatter diffraction (EBSD) studies to characterize grain size and orientation for different parts of the weld and the welding environment. Energy-dispersive spectroscopy (EDS) has been used to detect the selected area's chemical composition and produce composition mapping. These techniques for microstructural characterization and chemical analysis are summarized in Table 2.

Note that the two light optical microscopy techniques were abbreviated LOM-B and LOM-K for the two etchants used, namely, Barker's and Keller's. The three scanning electron microscopy techniques will be abbreviated SEM
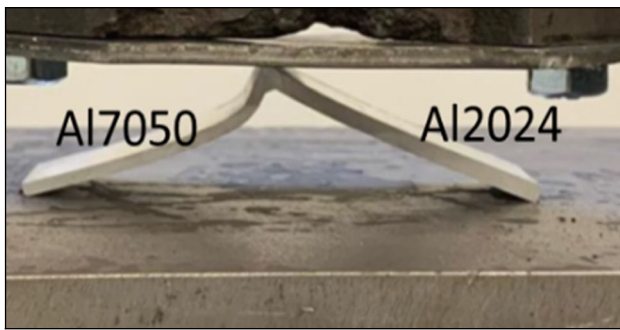
Fig. 6 The schematic image of the A- and B-type bending test setups

Fig. 7 Unconventional A-type bending of one side of the fillet weld under compressive loading, with the AA7050 side in tension
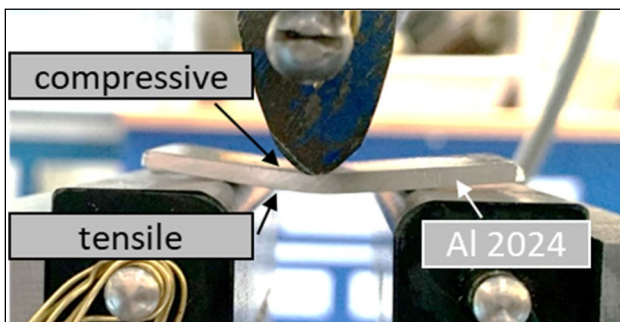

Fig. 8 Unconventional B-type bend test, with the T vertical member (AA7050), machined off, exposing the interface between the welding passes to tensile loading

SE, SEM BSE, and SEM EBSD for secondary electron imaging, backscattered electron imaging, and backscattered electron diffraction.

3 Results and discussion

3.1 Static T-pull test

The average values of the tensile strengths (R_m) of the base alloys AA7050 and AA2024 from uniaxial tensile testing

of the T-joints are shown in Fig. 9. The maximum error between the measured tensile strength values was 8%. The similarly determined data for the laser-welded (LBW) T-joint of the same base materials and the joint efficiency are also shown. The joint efficiency is the ratio between the strength of the weld and the base material (AA7050) multiplied by 100. The strength of the joint created with CSS-FSW exceeds that of the lower-strength base material (AA2024).

The CSS-FSW can be seen as having higher strength than the weaker member AA2024 and also achieving joint efficiencies in the 85–92%, especially after the post-weld aging treatments used. The CC-FSW also outperformed laser beam welding (LBW) for the same corner joint configuration.

3.2 Microstructural examination of the joint

The location of the samples used for microstructural analysis is shown in Fig. 10. Two parallel cross-sectional samples (a and b) were extracted from sections welded at different tilting angles (0.5°; 1°; 1.5°). The cross-sections of the CSS-FSW fillet welds using Barker's etching are shown in Fig. 11. Note the distinct contrast between the stir zone (SZ), heat-affected zones (HAZ), and base metal (BM) microstructures. Varying the angle of the probe did not make a significant difference in the weld quality, although, in terms of process optimization, this angle was an important process parameter. The FSW tilt angle is measured between the perpendicular axis to the welding direction, zero meaning identical to it. The V-shaped shoulder is geometrically constrained by the two parts being welded. It was found that the traverse force was significantly higher than for an equivalent butt joint with the same probe length. Furthermore, weld flash could get trapped ahead of the shoulder, further increasing the traverse forces. These force peaks were causing the machine to stall and the weld had to be aborted. The traverse force could be reduced by increasing the tilt angle from 0.5 to 1.5°, which reduced the overall contact area between the tool and the welded parts and allowed the tool to 'ride' over any flash built up ahead of the shoulder.

Table 2 Summary of metallographic features revealed by each analytical technique

Technique	Feature / Analysis					
	Composition	Grain size	Secondary phases	Texture	Flow lines	Fracture
LOM Keller's			X			
LOM Barker's		X	X	x	x	
SEM SE			X			x
SEM BSE	X		X			x
SEM EBSD		X		x		
EDS (point, map)	x		x			

Fig. 9 Comparison of tensile test data and joint efficiency for base materials, LBW, and FSW in the as-welded and different PWHT conditions
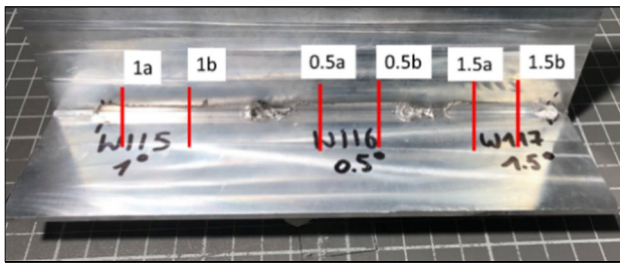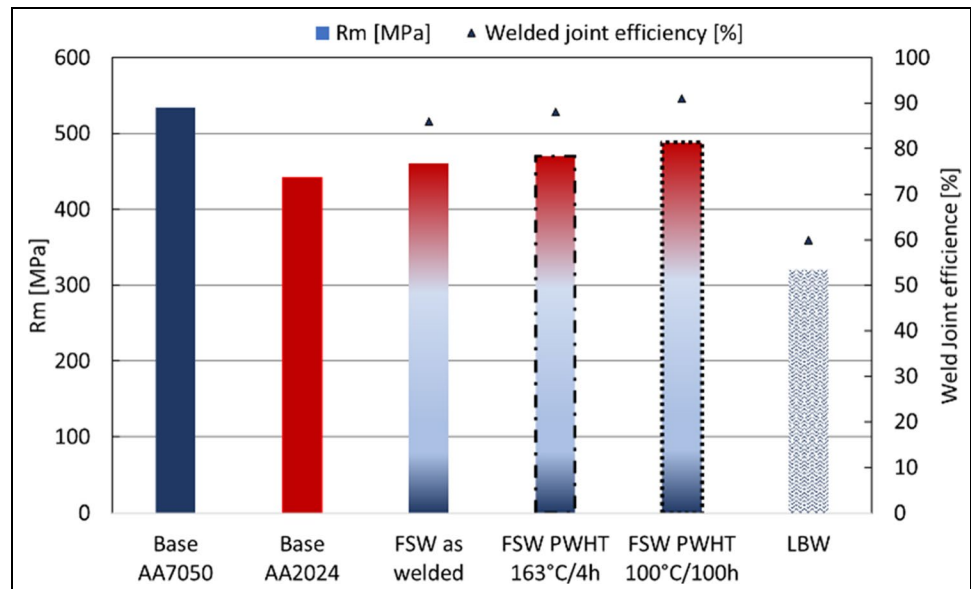

Fig. 10 Sampling (1a; 1b; 0.5a; 0.5b; 1.5a; 1.5b) for microstructure investigations regarding the probe angle 0.5°; 1°; 1.5°

opposed to the Cu-rich area (dark) zone within the first welding pass (right side of the weld). In the LM picture, the stir zone on the AA2024 side is barely visible, but the Zn-rich side of the stir zone is very sharp.

The information gathered from the above three methods can be considered complementary, as LOM-B reveals grain structure and flow lines but does not show precipitates or inclusions. LOM-K reveals the inclusions, but the image contrast is inadequate for estimating grain size or flow line. The SEM BSE imaging technique seems the best to show the size and distribution of precipitates and inclusions.

The extent to which the two alloys are mixed is best illustrated by the distribution of the dominant alloying elements. The distribution of the main alloying elements such as Zn, Cu, and Al in the stir zone can be visualized most convincingly by SEM–EDS maps. The example for the 1.b sample is shown in Fig. 13. The differences between the Al weld's Zn-rich and Cu-rich regions became more prominent. The penetration of the Zn-rich AA7050 material into the Cu-rich AA2024 appears obvious. It can be considered an adequate mechanical mixing in solid-state welding, unlike dilution in fusion welding, where melting and

As seen in Fig. 11, Barker's etching effectively revealed grain structure and grain size in both welds and base metals. The AA2024 exhibited an equiaxed and fine-grained structure, while the AA7050 vertical member parts showed more elongated grains following the initial rolling direction.

Keller's etching provided results similar to the SEM BSE image by being more sensitive to compositional differences in the weld (Fig. 12). Note the signs of mechanical mixing between the Zn-rich (light) areas of the FSW fillet weld, as

Fig. 11 Light microscopy images of the cross-section of CSS-FSW bonds with different probe angles (0.5°; 1°; 1.5°). Barker's etch, polarized light
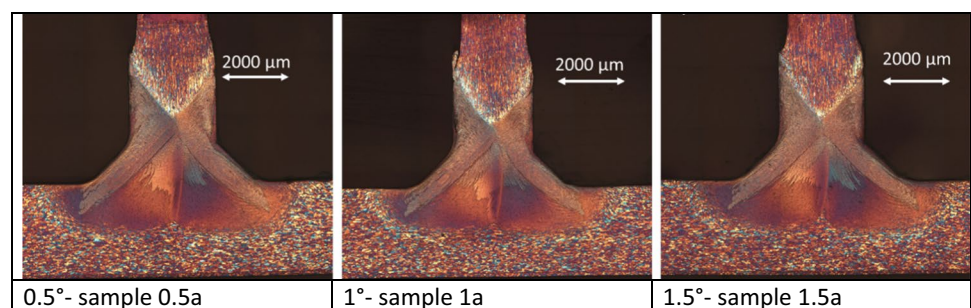

| 0.5°- sample 0.5a | 1°- sample 1a | 1.5°- sample 1.5a |

Fig. 12 **a** Microscopy images of CSS-FSW 1.b sample; **b** LOM Keller's etch SEM BSE image
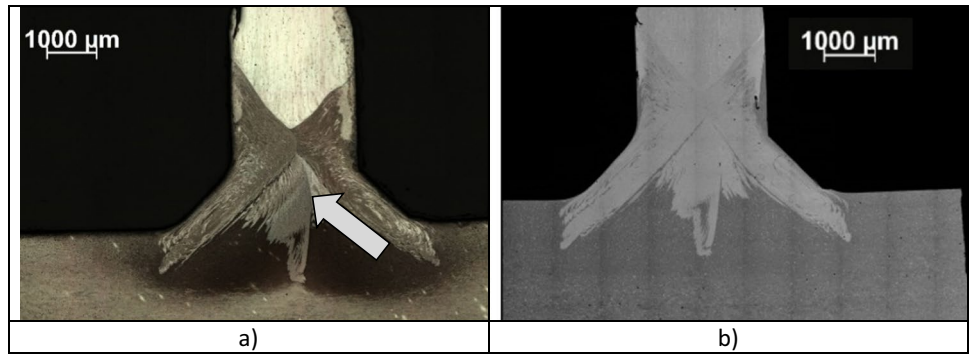

| a) | b) |

Fig. 13 EDS mapping of Al, Cu, and Zn in the stir zone of 1.b sample showing the "penetration" of Zn-rich AA7050 material into the Cu-rich AA2024

| Al (blue) | Cu (red) | Zn (green) |
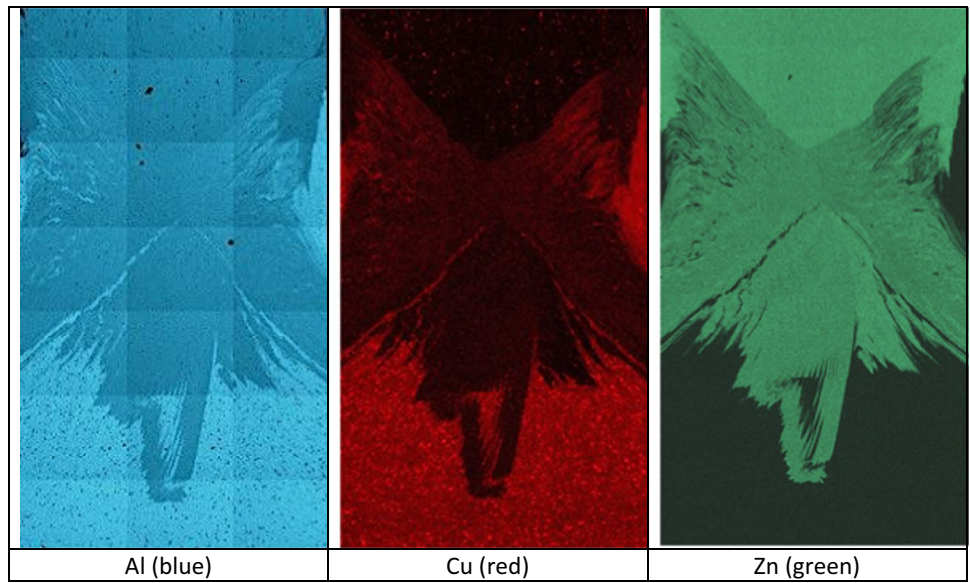
solidification occur. The relative amount of Zn-rich and Cu-rich zones in the SZ is about 50–50%. The chemical heterogeneity only indicates the direction of metal flow during FSW. It does not translate into microstructure or

Fig. 14 EBSD maps from the different parts of the 1.b. sample. Selected areas are indicated on Barker's image. Note that the magnification is different

Fig. 15 Barker's and SEM BSE images of the stir zone of 1.b sample. Selected EBSD maps are indicated on the SEM BSE image no. 7–10. Note that the EBSD maps' magnification is the same. The orientation index's legend is the same as in the upper right corner of Fig. 14
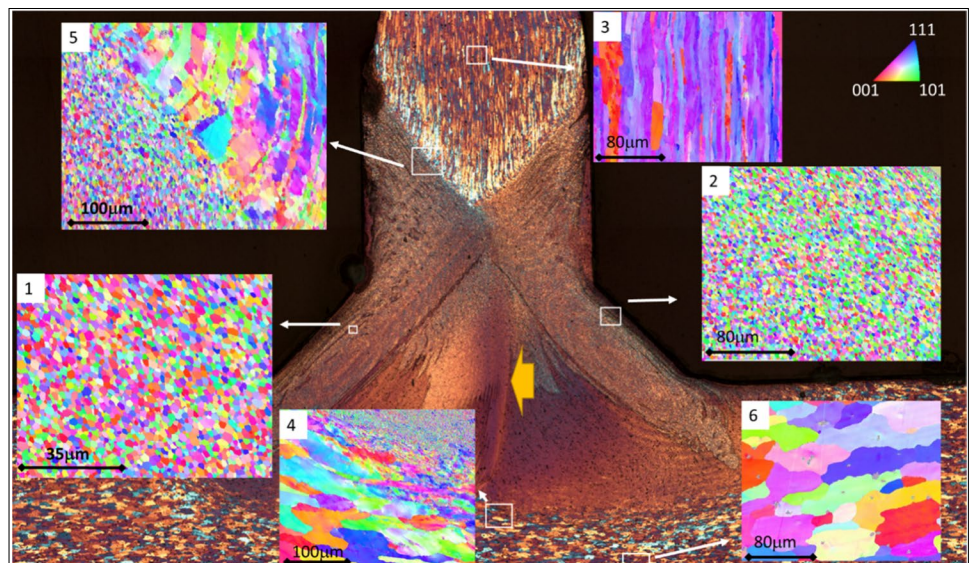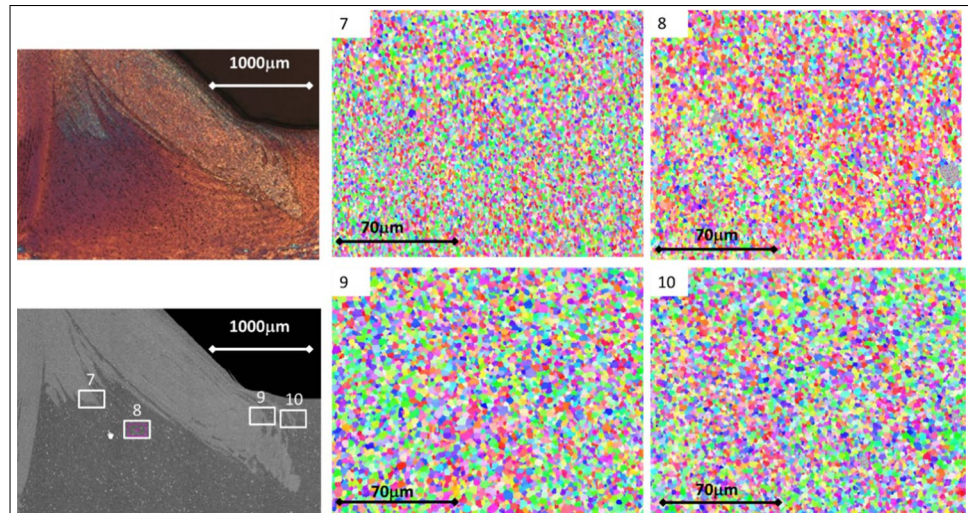
property differences in the stir zone. These images suggest that the Al-Cu alloy dominated the stir zone more, and the post-weld heat treatment response confirms this assumption.

To better understand the stir zone grain structure and reveal the plastic deformation processes, more particular area EBSD maps were produced (Fig. 14). The white squares represent the map's location on Barker's etching image and show the proportions of the EBSD mapped area. The magnifications are different because they are adjusted for the examined microstructural element. The orientation index is shown in the upper right corner.

The EBSD results clearly show that the AA2024 alloy (map No.6) is homogeneous grain size, showing equiaxed grains of 80–100 microns in length and isotropic with random orientation. Inside the grains, small non-indexed parts are visible; these are precipitates.

In contrast, AA7050 alloy consists of elongated, oriented grains (map No.3), with a predominant value between (001) and (111) orientation, likely remnants of the rolling process. EBSD maps also provide information on the boundary between the stir zone and the base alloys (map no. 5 and no. 4). The mixing of the fine-grained structure of the area with the coarse-grained structure

of the parent alloys is very well observed not only at the elemental level, seen earlier, but also clearly observed here at the grain level. The heat-affected zone consists of refined grains and mostly coarse grains. Extreme grain refinement has developed (map nos. 1 and 2), with homogeneous 1–3 micron mainly equiaxed grains. The orientation is typically random, with a weak (001) on the left (map no. 1) and a (101) dominance on the right side (map no. 2). In the morphological orientation of the grains, the direction of the material flow can also be inferred.

The yellow arrow highlights the overlap in the stir zone between the first (right side) and second (left side) pass.

Barker's etching technique highlights (see yellow arrow in Fig. 14) the overlap between the first and second welding pass in the stir zone, an area suspected of being a lack of bond or an oxide inclusion. The unconventional bending test of type B was used to investigate the weakness of this zone. A more detailed examination of the structure of the stir zone was also carried out, with particular attention to those parts that gave contrasts with different chemical compositions in the SEM BSE images. Figure 15 shows Barker's image of the stir zone of sample 1b and the SEM BSE image of the exact location. The

Fig. 16 Results of unconventional A-type bending test. **a** The red line indicates the sampling for Barker's image, **b** side view, **c** Barker's images
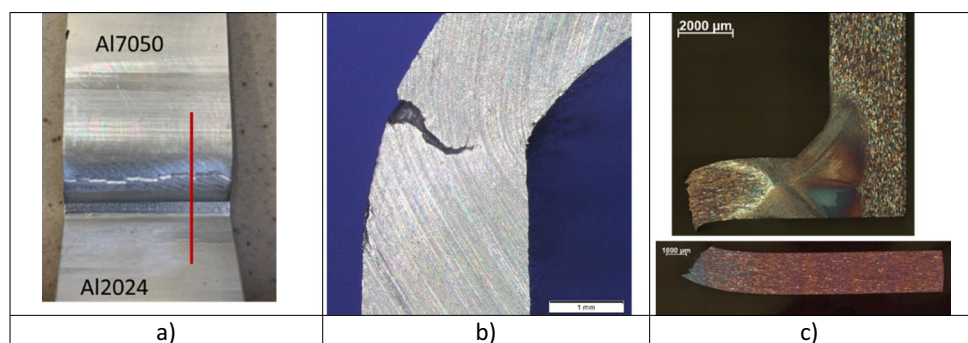
Fig. 17 Fractured sample subjected to unconventional B-type bend test with the T vertical member machined off, and this side subjected to tensile loading. **a** After the test (red lines: metallography cross-section), **b** sample position to SEM fracture analysis

a)

b)
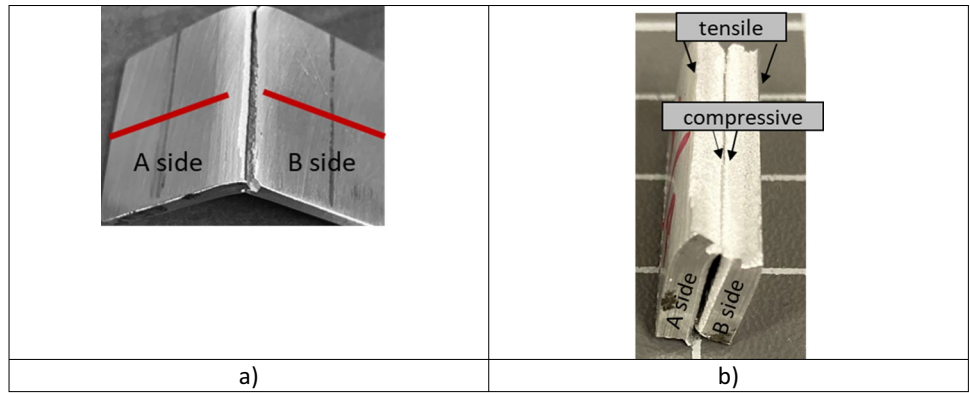
Fig. 18 SEM image of the fracture surface after the unconventional type B bending test. **a**) SE image of the B- and A-sides of the fractured sample, **b**) BSE image of the B- and A-sides (same area as a)), **c**) SE image of the B-side of the fractured sample, **d**) BSE image of the B-side (same area as c)), SE image of the A-side of the fractured sample, **e**) BSE image of the A-side (same area as d))

a)

b)

c)

d)

e)

f)

Fig. 19 SEM image of the B-side fracture surface after the unconventional B-type bending test, showing Cu-rich inclusion in the stir zone

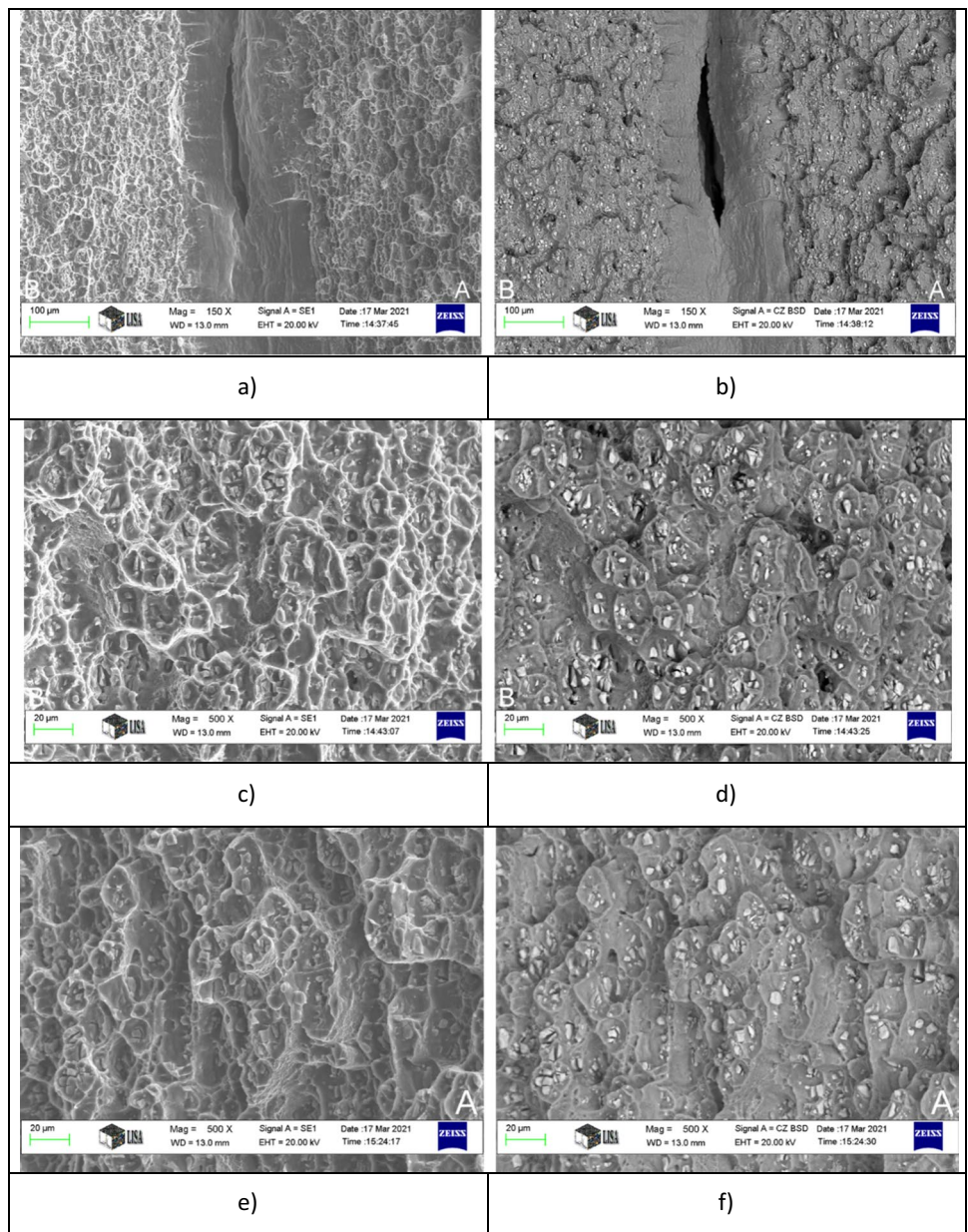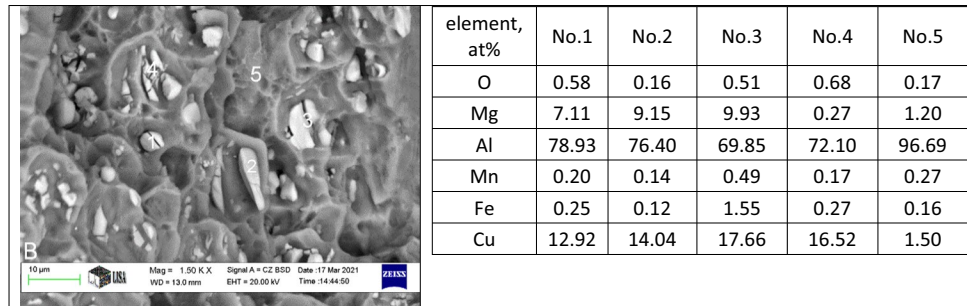| element, at%	No.1	No.2	No.3	No.4	No.5
O	0.58	0.16	0.51	0.68	0.17
Mg	7.11	9.15	9.93	0.27	1.20
Al	78.93	76.40	69.85	72.10	96.69
Mn	0.20	0.14	0.49	0.17	0.27
Fe	0.25	0.12	1.55	0.27	0.16
Cu	12.92	14.04	17.66	16.52	1.50

EBSD maps of the areas marked no. 7–no. 10 in the BSE image are shown at the same magnification.

The orientation index's legend is the same as in the upper right corner of Fig. 14. The EBSD signal of the different contrast parts does not differ in area no. 9 and no. 10. The grain size and the nature of the orientation are also very similar. Area no. 8, which is chemically more homogeneous, shows a slightly more dominant (001) texture and finer grain size than these.

Further refinement of grain size occurs in the chemically heterogeneous area no. 7. This particularly fine-grain structure is likely because the second weld pass was performed on the left side in this image, further refining the root of the initial first pass.

3.3 Unconventional bending tests

As a reminder, both A- and B-type unconventional tests were performed to force failure in areas that appeared to be problematic in the initial metallography evaluations. The B-type test was discussed above, so the A-type unconventional bending test specimen and Barker's image of the specimen's cross-section are shown in Fig. 16. The fracture can be seen originating far from the weld zone following large plastic deformation. The fracture was formed on the side of the AA7050 alloy HAZ, which has a smaller cross-section.

Again, the purpose of the B-type bending test was to examine the oxide-like inclusion at the overlap between the first and the second welding passes (yellow arrow Fig. 14). The cracked sample after the test and the position during the SEM examination can be seen in Fig. 17. The SEM tests carried out on the fractured surface are shown in Fig. 18. The SE images clearly show that the weld exhibits good ductility, but BSE images highlight many inclusions in the same area. There is no detectable difference in the A and B sides of the fracture. The point analysis performed on the high-magnification image shows that the inclusions are copper-rich intermetallic from the AA2024 BM like Al (Fe, Mn, Mg, Cu) (Fig. 19). Figure 20 and Fig. 21 show low-magnification cross-sectional images of the crack environment for both sides. The crack zones behave the same microstructural character as the block plate, with many evenly distributed copper-rich precipitates. Figure 22
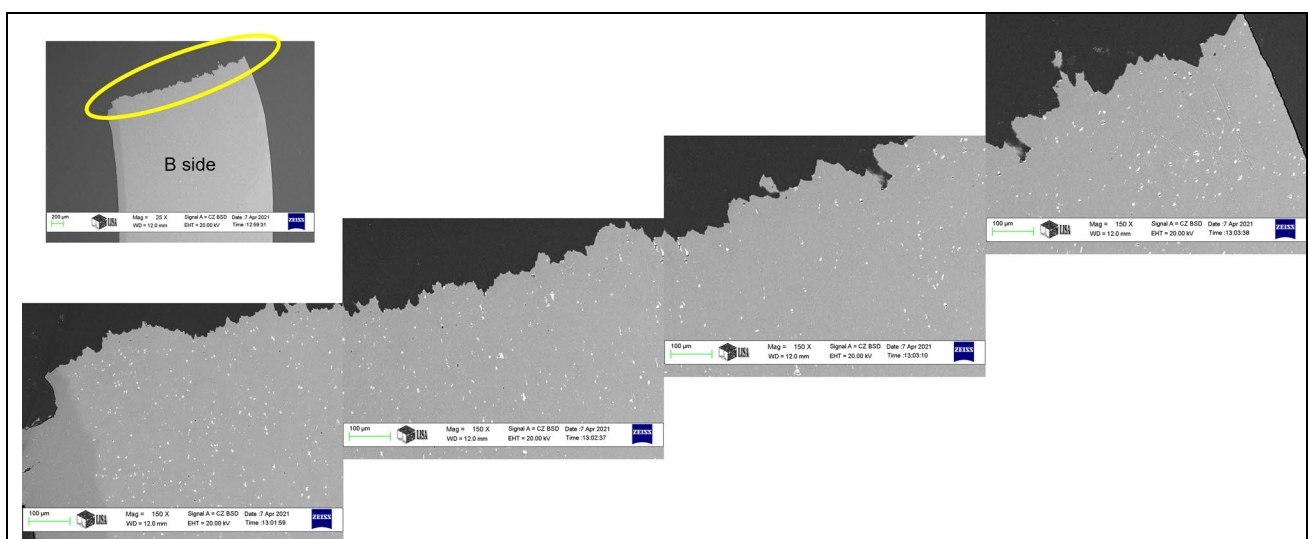

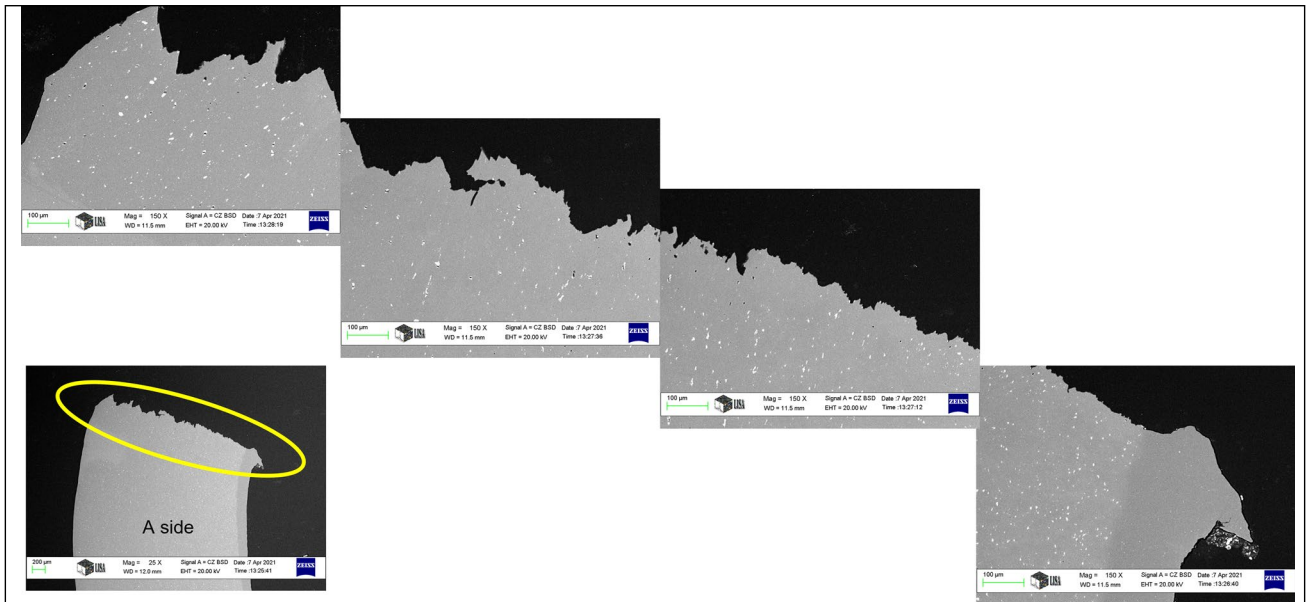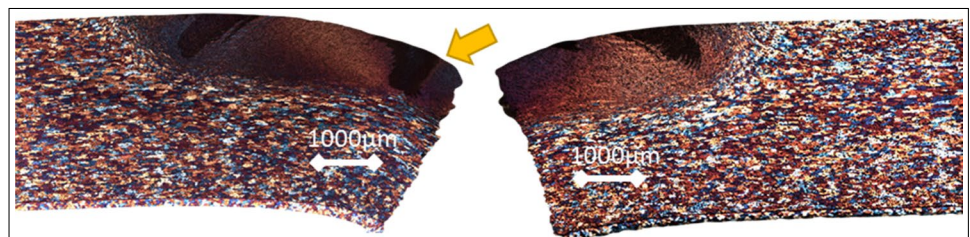**Fig. 20** Fracture surface profile SEM image of the B-side cross-section

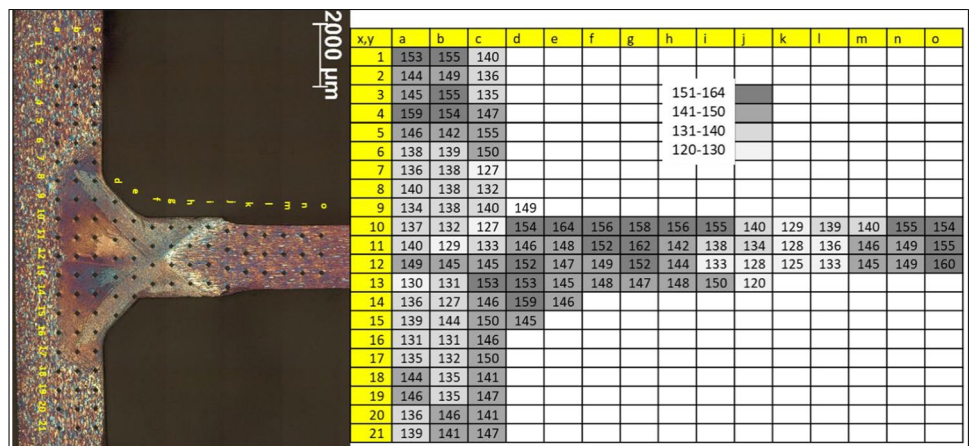**Fig. 21** Fracture surface profile SEM image of the A-side cross-section

Fig. 22 Results of unconventional B type bending test. A- and B-side cross-section Barker's image. The yellow arrow indicates the overlap in the stir zone between the first (right side) and second (left side) pass

shows Barker's image's A and B side cross-section after the unconventional B-type bending test. The yellow arrow highlights the overlap in the stir zone between the first (right side) and second (left side) pass. There is clear evidence that the fracture crack did not occur at the first and second pass boundary indicated by the yellow arrow.

Overall, it can be concluded that neither of the discontinuities suspected initially were responsible for fractures, even though these unconventional destructive tests could have likely forced failure in those locations. Therefore, the actual CSS-FSW welds can be assumed to have excellent integrity based on the thorough examination of these welded coupons.

Fig. 23 HV0.1 mapping of sample 0.5a. Four grades greyscale

x,y	a	b	c	d	e	f	g	h	i	j	k	l	m	n	o
1	153	155	140												
2	144	149	136												
3	145	155	135					151-164							
4	159	154	147					141-150							
5	146	142	155					131-140							
6	138	139	150					120-130							
7	136	138	127												
8	140	138	132												
9	134	138	140	149											
10	137	132	127	154	164	156	158	156	155	140	129	139	140	155	154
11	140	129	133	146	148	152	162	142	138	134	128	136	146	149	155
12	149	145	145	152	147	149	152	144	133	128	125	133	145	149	160
13	130	131	153	153	145	148	147	148	150	120					
14	136	127	146	159	146										
15	139	144	150	145											
16	131	131	146												
17	135	132	150												
18	144	135	141												
19	146	135	147												
20	136	146	141												
21	139	141	147												

3.4 Hardness measurement results

The mechanical homogeneity of the weld was verified by HV0.1 mapping. The results of sample 0.5a can be seen in Fig. 23. The x y coordinates are yellow in Barker's picture and the table. Black diamonds clearly show where the measurements were taken. The hardness varies between 120 and 164 values, so four grades of greyscale highlight the distribution. The more significant hardness value is dominant at the base materials and in the outer part of the mixing zone. A softening happens in the inner part and the heat-affected zone. Comparing Fig. 17 and Fig. 23, the crack did not occur in the lower hardness heat-affected zone.

4 Conclusions

Based on the extensive characterization of several CSS-FSW of dissimilar aluminum welded coupons, it can be concluded that:

- Traditional etching and EDS elemental mapping in the SEM of dissimilar joints can sometimes result in erroneous interpretation of the weld integrity because of the apparent chemical heterogeneity and oxide-like inclusions in the FSW stir zone.
- On the other hand, color metallography and EBSD can add clarifying details to these questionable interpretations. Indeed, the joint strength exceeded that of the lower-strength base material (AA2024), reaching up to 92% joint efficiency compared to the higher strength member (AA7050).
- Unconventional bend testing and hardness mapping pointed out that the fracture occurred far from the weld and the heat-affected zone. The fracture initiation occurred in the thinner aluminum member, and no other failure was initiated in the initially suspect areas, which appeared as oxide inclusions.
- The CSS-FSW technique produced good mixing between the two base metals. The composition maps suggest that the stir zone was more dominated by the aircraft skin's AA2024 Al-Cu alloy skin than the stiffener AA7050 Al-Zn alloy.
- The stir zone exhibited a homogenous, equiaxed, fine-grained harder structure, while the heat-affected zone consisted of softer, coarser grains on both aluminum base metal sides.

5 Recommendations

Based on the analysis of the above welded coupons, the following recommendations can be made:

- Avoid the thickening of the weld in the area of the stiffener by reducing the size of the "elephant foot" joint preparation (Fig. 3) from the current 1.5×1.5 mm to 1.0×1.0 mm. Alternately, make a groove in the thickened part of the aircraft skin.
- Grind smooth (dress) the vertical AA7050 member weld in the HAZ zone on both sides of the stiffener. This would be needed to remove the geometric stress concentration due to the local thickening of the weld.
- Consider post-weld heat treatment (PWHT) to further improve the weld strength by using local induction heating at low temperatures (100 °C) and long times (100 h) to avoid distortions of the part. Welded joint efficiency of up to 95% could be achieved this way.

Acknowledgements Special thanks go to Dr. Petr Homola from VLZU Prague, Czech Republic, for sharing some of the mechanical test results. This research was part-funded by the OASIS Project (GA 785557) funded by the Horizon Europe framework, Clear Sky 2. Finally, we would like to thank SAAB Aerostructures, Sweden, for allowing us to publish their data. The research was conducted at the University of Miskolc as part of the "Developments aimed at increasing social benefits deriving from more efficient exploitation and utilization of domestic subsurface natural resources" project supported by the Ministry of Innovation and Technology from the National Research, Development and Innovation Fund according to the Grant Contract issued by the National Research, Development and Innovation Office (Grant Contract reg. nr.: TKP-17-1/PALY-2020). Parts of this paper have been supported by the National Research, Development and Innovation Office – NKFIH, OTKA PD 138729.

Funding Open access funding provided by Budapest University of Technology and Economics.

Declarations

All authors agree with the participation and publication of this article. We declare that we do not have any commercial or associative interest that represents a conflict of interest in connection with the work submitted.

Open Access This article is licensed under a Creative Commons Attribution 4.0 International License, which permits use, sharing, adaptation, distribution and reproduction in any medium or format, as long as you give appropriate credit to the original author(s) and the source, provide a link to the Creative Commons licence, and indicate if changes were made. The images or other third party material in this article are included in the article's Creative Commons licence, unless indicated otherwise in a credit line to the material. If material is not included in the article's Creative Commons licence and your intended use is not permitted by statutory regulation or exceeds the permitted use, you will need to obtain permission directly from the copyright holder. To view a copy of this licence, visit http://creativecommons.org/licenses/by/4.0/.

References

1. Christner B, McCoury J, Higgins S (2003) Development and testing of friction stir welding (FSW) as a joining method for primary

aircraft structure. In: Proceedings of 4th International Symposium on Friction Stir Welding. Park City, TWI, pp 57–68

2. Huang L, Hua X, Wu D (2018) Relationship between the weld pool convection and metallurgical and mechanical properties in hybrid welding for butt joint of 10-mm-thick aluminum alloy plate. Weld World 62:895–903. https://doi.org/10.1007/s40194-018-0591-9

3. Ribeiro RA, Assunção PDC, Dos SEBF et al (2020) An overview on the cold wire pulsed gas metal arc welding. Weld World 64:123–140. https://doi.org/10.1007/s40194-019-00826-w

4. Van Haver W, Stassart X, Verwimp J et al (2006) Friction stir welding and hybrid laser welding applied to 6056 alloy. Weld World 50:65–77. https://doi.org/10.1007/BF03263463

5. Sajadifar SV, Moeini G, Scharifi E et al (2019) On the effect of quenching on postweld heat treatment of friction-stir-welded aluminum 7075 alloy. J Mater Eng Perform 28:5255–5265. https://doi.org/10.1007/s11665-019-04252-3

6. Zhao P, Tang H, Lin S et al (2019) Effect of local postweld heat treatments on metal inert gas-welded a7n01s-t5 joints. J Mater Eng Perform 28:3622–3629. https://doi.org/10.1007/s11665-019-04128-6

7. Çam G, Mistikoglu S (2014) Recent developments in friction stir welding of al-alloys. J Mater Eng Perform 23:1936–1953. https://doi.org/10.1007/s11665-014-0968-x

8. Saha R, Biswas P (2022) Current status and development of external energy-assisted friction stir welding processes: a review. Weld World. https://doi.org/10.1007/s40194-021-01228-7

9. Mi S, Zhang Y, Fu X et al (2021) A measurement method of weld temperature and tool positioning during friction stir welding process. Weld World 65:1531–1540. https://doi.org/10.1007/s40194-021-01067-6

10. Saju TP, Narayanan RG, Roy BS (2021) Joining dissimilar grade aluminum alloy sheets using multi-hole dieless friction stir riveting process. Int J Adv Manuf Technol 112:285–302. https://doi.org/10.1007/s00170-020-06393-5

11. Bang HS, Lee WR, Hong SM et al (2018) Mechanical properties of dissimilar A356/SAPH440 lap joints by the friction stir spot welding and self-piercing riveting. Strength Mater 50:63–71. https://doi.org/10.1007/s11223-018-9943-3

12. Meng X, Xu Z, Huang Y et al (2018) Interface characteristic and tensile property of friction stir lap welding of dissimilar aircraft 2060–T8 and 2099–T83 Al–Li alloys. Int J Adv Manuf Technol 94:1253–1261. https://doi.org/10.1007/s00170-017-0996-4

13. Lumsden J, Pollock G, Mahoney MW (2003) The effect of thermal treatments on the corrosion behavior of friction stir welded 7050 and 7075 aluminum alloys. Mater Sci Forum 426–432:2867–2872. https://doi.org/10.4028/www.scientific.net/MSF.426-432.2867

14. Jata KV, Sankaran KK, Ruschau JJ (2000) Friction-stir welding effects on microstructure and fatigue of aluminum alloy 7050–T7451. Metall Mater Trans A 31:2181–2192. https://doi.org/10.1007/s11661-000-0136-9

15. Victor Christy J, Ismail Mourad A-H, Sherif MM, Shivamurthy B (2021) Review of recent trends in friction stir welding process of aluminum alloys and aluminum metal matrix composites. Trans Nonferrous Met Soc China 31:3281–3309. https://doi.org/10.1016/S1003-6326(21)65730-8

16. Su J-Q, Nelson T, Mishra R, Mahoney M (2003) Microstructural investigation of friction stir welded 7050–T651 aluminium. Acta Mater 51:713–729. https://doi.org/10.1016/S1359-6454(02)00449-4

17. Dumont D, Deschamps A, Brechet Y (2003) On the relationship between microstructure, strength and toughness in AA7050 aluminum alloy. Mater Sci Eng A 356:326–336. https://doi.org/10.1016/S0921-5093(03)00145-X

18. Russel MJ, Threadgill PL, Thomas MJ, Wynne BP (2007) Static shoulder friction stir welding of Ti–6Al–4V; process and evaluation. In: Niinomi M (ed) proceedings of the 11th World Conference on Titanium (JIMIC 5). Japan Institute of Metals, Kyoto

19. Patel V, Li W, Wen Q et al (2019) Stationary shoulder friction stir processing: a low heat input grain refinement technique for magnesium alloy BT - friction stir welding and processing X. In: Mishra R, Sato Y et al (eds) Hovanski Y. Springer International Publishing, Cham, pp 209–215

20. Goebel J, Reimann M, Norman A, dos Santos JF (2017) Semi-stationary shoulder bobbin tool friction stir welding of AA2198-T851. J Mater Process Technol 245:37–45. https://doi.org/10.1016/j.jmatprotec.2017.02.011

21. Patel V, Li W, Liu X et al (2019) Through-thickness microstructure and mechanical properties in stationary shoulder friction stir processed AA7075. Mater Sci Technol 35:1762–1769. https://doi.org/10.1080/02670836.2019.1641459

22. You J, Zhao Y, Dong C et al (2021) Numerical modeling of multiphysics field in conventional and stationary shoulder friction stir welding of Al-Cu alloy. J Mater Eng Perform 30:2751–2760. https://doi.org/10.1007/s11665-021-05642-2

23. Martin JP, Stanhope C, Gascoyne S (2011) Novel techniques for corner joints using friction stir welding. In Friction Stir Welding and Processing VI. Wiley, Hoboken, pp 179–186

24. Evans WT, Cook GE, Strauss AM (2017) Joining Aerospace Aluminum 2024–T4 to Titanium by Friction Stir Extrusion BT - Friction Stir Welding and Processing IX. In: Mishra R, Sato Y et al (eds) Hovanski Y. Springer International Publishing, Cham, pp 79–89

25. Shanavas S, Edwin Raja Dhas J, Murugan N (2018) Weldability of marine grade AA 5052 aluminum alloy by underwater friction stir welding. Int J Adv Manuf Technol 95:4535–4546. https://doi.org/10.1007/s00170-017-1492-6

26. Yue Y, Wang G, Yang K et al (2018) Friction stir butt welding thin aluminum alloy sheets. Int J Adv Manuf Technol 96:3139–3147. https://doi.org/10.1007/s00170-018-1798-z

27. Golezani AS, Barenji RV, Heidarzadeh A, Pouraliakbar H (2015) Elucidating of tool rotational speed in friction stir welding of 7020–T6 aluminum alloy. Int J Adv Manuf Technol 81:1155–1164. https://doi.org/10.1007/s00170-015-7252-6

28. Khoshnaw FM, Gardi RH (2007) Effect of aging time and temperature on exfoliation corrosion of aluminum alloys 2024–T3 and 7075–T6. Mater Corros 58:345–347. https://doi.org/10.1002/maco.200604008

29. Niu PL, Li WY, Li N et al (2019) Exfoliation corrosion of friction stir welded dissimilar 2024-to-7075 aluminum alloys. Mater Charact 147:93–100. https://doi.org/10.1016/j.matchar.2018.11.002

30. DeBacker J et al (2021) Optimization of Friction Stir Welding and Laser Beam Welding for Assembly of Structural Aircraft Parts. OASIS Final Report, Clear Sky 2 Europe Horizon Project GA 785557